J|A|C|S
ARTICLES
Published on Web 03/22/2006

$[Fe(bpym)(CN)_4]^-$: A New Building Block for Designing Single-Chain Magnets

Luminita Marilena Toma,[†] Rodrigue Lescouëzec,[†,§] Jorge Pasán,[‡] Catalina Ruiz-Pérez,[‡] Jacqueline Vaissermann,[§] Joan Cano,[⊥] Rosa Carrasco,[†] Wolfgang Wernsdorfer,[∥] Francesc Lloret,[†] and Miguel Julve*[,†]

Contribution from the Departament de Química Inorgánica/Instituto de Ciencia Molecular, Facultat de Química de la Universitat de València, Avda. Dr. Moliner 50, 46100 Burjassot, València, Spain, Laboratorio de Rayos X y Materiales Moleculares, Departamento de Física Fundamental II, Facultad de Física de la Universidad de La Laguna, Avda. Astrofísico Francisco Sánchez s/n, 38204 La Laguna, Tenerife, Spain, Laboratoire de Chimie Inorganique et Matériaux Moléculaires, Université Pierre et Marie Curie, F-75252 Paris, Cedex 05, France, Laboratoire Louis Néel, CNRS, BP 166, 25 Avenue des Martyrs, 38042 Grenoble Cedes 09, France, and Institució Catalana de Recerca i Estudis Avançats(ICREA)/Departament de Química Inorgànica i Centre de Recerca en Química Teórica, Universitat de Barcelona, Avda. Diagonal 647, 08028 Barcelona, Spain

Received December 12, 2005; E-mail: . miguel.julve@uv.es

Abstract: We herein present the preparation, crystal structure, magnetic properties, and theoretical study of new heterobimetallic chains of formula $\{[Fe^{III}(bpym)(CN_4)]_2M^{II}(H_2O)_2\}\cdot 6H_2O$ [bpym = 2,2′-bipyrimidine; M = Zn (**2**), Co (**3**), Cu (**4**), and Mn (**5**)] which are obtained by using the building block $PPh_4[Fe(bpym)(CN)_4]\cdot H_2O$ (**1**) (PPh_4^+ = tetraphenylphosphonium) as a ligand toward the fully solvated M^{II} ions. The structure of complex **1** contains mononuclear $[Fe(bpym)(CN)_4]^-$ anions. Compounds **2**−**5** are isostructural 4,2-ribbonlike bimetallic chains where the $[Fe(bpym)(CN)_4]^-$ unit acts as a bis-monodenate ligand through two of its four cyanide ligands toward the M atom. Water hexamer clusters (**4**) and regular alternating fused six- and four-membered water rings with two dangling water molecules (**2**, **3**, and **5**) are trapped between the cyanide-bridged 4,2-ribbonlike chains. **1** and **2** behave as magnetically isolated low-spin iron(III) centers. **3** behaves as a single-chain magnet (SCM) with intrachain ferromagnetic coupling, slow magnetic relaxation, hysteresis effects, and frequency-dependent ac signals at $T < 7$ K). As expected for a thermally activated process, the nucleation field (H_n) in **3** increases with decreasing T and increasing v. Below 1.0 K, H_n becomes temperature independent but remains strongly sweep rate dependent. In this temperature range, the reversal of the magnetization may be induced by a quantum nucleation of a domain wall that then propagates due to the applied field. **4** and **5** are ferro- and ferrimagnetic chains respectively, with metamagnetic-like behavior (**4**). DFT-type calculations and QMC methodology provided a good understanding of the magnetic properties of **3**−**5**.

Introduction

Magnetic systems that exhibit slow relaxation of the magnetization such as single-molecule magnets (SMMs)[1,2] and single-chain magnets (SCMs)[4−6] are very hot topics in chemistry and materials science because of the interest in them from a fundamental point of view (quantum phenomena and finite-size effects, for instance) and also because of their possible applications in magnetic devices (nanometric magnetic memory units).[7] A ground state with both high spin (S) and large negative axial anisotropy (D) together with negligible intermolecular interactions are the requirements to have a double minimum potential for the reversal of the magnetic moment in the so-called SMMs.

[†] Universitat de Valencia.
[‡] Universidad de La Laguna.
[§] Université Pierre et Marie Curie.
[⊥] ICREA and Universitat de Barcelona.
[∥] Laboratoire Louis Néel.

(1) (a) Sessoli, R.; Gatteschi, D.; Novak, M. A. *Nature* **1993**, *365*, 141. (b) Sessoli, R.; Tsai, H.; Schake, A. R.; Wang, S.; Vincent, J. B.; Folting, K.; Gattechi, D.; Christou, G.; Hendrickson, D. N. *J. Am. Chem. Soc*. **1993**, *115*, 1804.
(2) Gatteschi, D.; Sessoli, R. *Angew. Chem., Int. Ed.* **2003**, *42*, 268 and references therein.
(3) Winpenny, R. E. P. Adv. *Inorg. Chem.* **2001**, *1*, 52 and references therein.
(4) (a) Caneschi, A.; Gatteschi, D.; Lalioti, N.; Sangregorio, C.; Sessoli, R.; Venturi, G.; Vindigni, A.; Rettori, A.; Pini, M. G.; Novak, M. A. *Angew. Chem., Int. Ed.* **2001**, *40*, 1760. (b) Caneschi, A.; Gatteschi, D.; Lalioti, N.; Sessoli, R.; Sorace, L.; Tanngoulis, V.; Vindigni, A. *Chem. Eur. J.* **2002**, *8*, 286. (c) Caneschi, A.; Gatteschi, D.; Lalioti, N.; Sangregorio, C.; Sessoli, R.; Venturi, G.; Vindigni, A.; Rettori, A.; Pini, M. G.; Novak, M. A. *Europhys. Lett.* **2002**, *58*, 771. (d) Bogani, L.; Caneschi, A.; Fedi, M.; Gatteschi, D.; Massi, M.; Novak, M. A.; Pini, M. G.; Rettori, A.; Sessoli, R.; Vindigni, A. *Phys. Rev. Lett.* **2004**, *92*, 207204.
(5) (a) Clérac, R.; Miyasaka, H.; Yamashita, M.; Coulon, C. *J. Am. Chem. Soc.* **2002**, *124*, 12387. (b) Miyasaka, H.; Clérac, R.; Mizushima, K.; Sugiura, K.; Yamashita, M.; Wernsdorfer, W.; Coulon, C. *Inorg. Chem.* **2003**, *42*, 8203.
(6) Lescouëzec, R.; Vaissermann, J.; Ruiz-Pérez, C.; Lloret, F.; Carrasco, R.; Julve, M.; Verdaguer, M.; Dromzee, Y.; Gatteschi, D.; Wernsdorfer, W. *Angew. Chem., Int. Ed.* **2003**, *42*, 1483.
(7) (a) Wernsdorfer, W.; Sessoli, R. *Science* **1999**, *284*, 133. (b) Leuenberger, M. N.; Loss, D. *Nature* **2001**, *410*, 789.

 10.1021/ja058030v CCC: $33.50

The interest in the SCMs has its origin in Glauber's early theoretical work.[8] He suggested that the conditions needed to observe slow magnetic relaxation in a one-dimensional compound were: (i) it must behave as an Ising ferro- or ferrimagetic chain and (ii) the ratio J/J' has to be larger than 10^4 (J and J' being the intrachain and interchain magnetic interactions, respectively). More than three decades were needed to observe this behavior for the first time because of these rather stringent requirements. The ferrimagnetic chain $[Co^{II}(hfac)_2(NITPhOMe)]$ (Hhfac = hexafluoroacetylacetone and NITPhOMe = 4′-methoxy-phenyl-4,4,5,5-tetramethylimidazoline-1-oxyl-3-oxide) was the first example of this type of system reported by Gatteschi et al. in 2001.[3a] The alternating current (ac) magnetic susceptibility of this compound is strongly field dependent below 17 K, and the relaxation time (τ) shows a thermally activated (Arrhenius) behavior with $\tau_o = 3.0 \times 10^{-11}$ s and an energy barrier (E_a) to reverse the magnetization of 107 cm^{-1}. The anisotropy of high-spin cobalt(II)-radical intrachain exchange interaction gives the barrier for the reorientation of the magnetization. The first heterometallic SCMs were reported in 2002 by Clérac et al. and they deal with a family of bimetallic chains of general formula $[Mn^{III}_2(saltmen)_2Ni^{II}(pao)_2L_2]A_2$ [saltmen^{2-} = *N*,*N*′-(1,1,2,2-tetramethylene)bis(salicylideneiminate), pao$^-$ = pyridine-2-aldoximate, L = nitrogen donor heterocycle, and A^- = univalent anion] where regular alternating single oximato bridges between Ni^{II} and Mn^{III} (antiferromagnetic coupling) and double phenolate-oxo bridges between pairs of Mn^{III} ions (ferromagnetic coupling) occur.[4] Coercivity and relaxation of the magnetization below 3.5 K are observed in this family. Other more recent examples of SCMs are the homospin helical chain $[Co^{II}(bt)(N_3)_2]$ (bt = 2,2′-bithiazoline) with double end-on azido bridges between the high-spin cobalt(II) ions,[9] the oxamidato-bridged heterobimetallic chain $[Co^{II}Cu^{II}(2,4,6\text{-tmpa})_2(H_2O)_2]\cdot 4H_2O$ (2,4,6-tmpa^{2-} = *N*-2,4,6-trimethylphenyloxamate dianion),[6] the Mn_7 clusters $[Mn_7O_8(O_2SePh)_8(O_2CMe)(H_2O)]$ and $[Mn_7O_8(O_2SePh)_9(H_2O)]$[10] and the mixed 3d/4f chain compound $(LCu)_2Tb(NO_3)(H_2O)$ [H_3L = 2-hydroxy-*N*-{2-[(2-hydroxyethyl)amino]ethyl}benzamide).[11]

Our team, among others, is engaged in the extension of the work on SCMs to the cyanide-bearing compounds by using the so-called bottom-up synthetic approach.[6,12−14] Our rational design of SCMs is based on a careful choice of the building block (a paramagnetic cyanide-containing metal complex). In this respect, we prepared the $[M^{III}(AA)(CN_4)]^-$ mononuclear species (M = Cr and Fe; AA = bidentate nitrogen donor),[15,16] and we explored their use as ligands toward fully solvated first-row transition metal ions (M′)[6,12,15a,b,16] and partially blocked complexes.[15c,17] Among the different cyano-bridged polynuclear compounds obtained, the single and double 4,2-ribbonlike heterobimetallic chains with M = Fe(III) and M′ = Co(II) and Cu(II) exhibit intrachain ferromagnetic coupling and the typical behavior of the SCMs.[6,12]

In the present work, we focus on the preparation, crystal structure determination, magnetic investigation, and theoretical study of the new cyanide-bearing precursor $PPh_4[Fe^{III}(bpym)(CN)_4]\cdot H_2O$ (**1**) (PPh_4^+ = tetraphenylphosphonium and bpym = 2,2′-bipyrimidine) and of the heterobimetallic chains of formula $\{[Fe^{III}(bpym)(CN_4)]_2M^{II}(H_2O)_2\}\cdot 6H_2O$ [bpym = 2,2′-bipyrimidine; M = Zn (**2**), Co (**3**), Cu (**4**), and Mn (**5**)]. **3** is a new example of SCM whose reversal of the magnetization is analyzed by a model of thermally activated nucleation on the basis of magnetization measurements on a single crystal at very low temperatures.

Experimental Section

Materials. Chemicals were purchased from commercial sources, and they were used without further purification. Elemental analyses (C, H, N) were carried out at the Microanalytical Service of the Universidad Autónoma de Madrid. Fe/P (**1**), and Fe/M [M = Zn (**2**), Co (**3**), Cu (**4**), and Mn (**5**)] molar ratios of 1:1 (**1**) and 2:1 (**2**−**5**) were determined by electron probe X-ray microanalysis at the Servicio Interdepartamental de la Universitat de València.

WARNING. The severe toxicity of cyanide and most of its compounds must be taken into account in the laboratory. Our syntheses were performed at millimolar scale in a hood, and the samples were handled with great caution.

Synthesis of the Complexes. $PPh_4[Fe^{III}(bpym)(CN)_4]\cdot H_2O$ (1). Compound **1** was prepared by following a procedure similar to that described for the related compounds with 2,2′-bipyridine or 1,10-phenanthroline instead of bpym in refs 15a,b. X-ray-quality dark-red prisms of **1** were obtained by recrystallization of the crude product from a H_2O/MeOH (1:1) mixture. Yield is 54%. Anal. Calcd for $C_{36}H_{28}FeN_8OP$ (**1**): C, 64.03; H, 4.15; N, 16.59. Found: C, 63.50; H, 4.01; N, 16.25. IR (KBr pellets): ν (cyanide stretching) = 2124(m) and 2112(m) cm^{-1}.

$\{[Fe^{III}(bpym)(CN_4)]_2M^{II}(H_2O)_2\}\cdot 6H_2O$ (2−5). X-ray-quality crystals of compounds **2**−**4** were obtained by slow diffusion in an H-tube of aqueous solutions of $Li[Fe(bpym)(CN)_4]$ [isolated by methatetic reaction of **1** and $LiClO_4\cdot H_2O$ in a 1:1 molar ratio (0.2 mmol) in acetonitrile] in one arm and the corresponding nitrate salt (0.1 mmol) $[Zn(NO_3)_2\cdot 6H_2O$ (**1**), $Co(NO_3)_2\cdot 6H_2O$ (**3**), $Cu(NO_3)_2\cdot 3H_2O$ (**4**), and $Mn(NO_3)_2\cdot 4H_2O$ (**5**)] in the other arm. The diffusion was allowed to proceed in the dark, and well-shaped orange (**2** and **5**) and brown (**3**) prisms and maroon plates (**4**) were obtained. The yield is practically quantitative after a few weeks. Anal. Calcd for $C_{24}H_{28}Fe_2N_{16}O_8Zn$ (**2**): C, 36.51; H, 3.55; N, 28.37. Found: C, 36.28; H, 3.45; N, 28.19. Anal. Calcd for $C_{24}H_{28}CoFe_2N_{16}O_8$ (**3**): C, 36.82; H, 3.58; N, 28.62. Found: C, 36.55; H, 3.49; N, 28.48. Anal. Calcd for $C_{24}H_{28}CuFe_2N_{16}O_8$ (**4**): C, 36.60; H, 3.55; N, 28.44. Found: C, 36.49; H, 3.43; N, 28.17. Anal. Calcd for $C_{24}H_{28}Fe_2MnN_{16}O_8$ (**5**): C, 37.00; H, 3.59; N, 28.75. Found: C, 36.87; H, 3.49; N, 28.61. IR (KBr pellets): ν(cyanide stretching) = 2174(m), 2124(w), and 2114(w) (**2**), 2171(m), 2126(w), and 2113(w) (**3**), 2186(m) and 2117(w) (**4**), and 2157(m) and 2132(w) cm^{-1} (**5**).

(8) Glauber, R. J. *J. Math. Phys.* **1963**, *4*, 294.
(9) Liu, T. F.; Fu, D.; Gao, S.; Zhang, Y. Z.; Sun, H. L.; Su, G.; Liu, Y. J. *J. Am. Chem. Soc.* **2003**, *125*, 13976.
(10) Chakov, N. E.; Wernsdorfer, W.; Abboud, K. A.; Christou, G. *Inorg. Chem.* **2004**, *43*, 5919.
(11) Costes, J. P.; Clemente-Juan, J. M.; Dahan, F.; Milon, J. *Inorg. Chem.* **2004**, *43*, 8200.
(12) (a) Toma, L. M.; Lescouëzec, R.; Lloret, F.; Julve, M.; Vaissermann, J.; Verdaguer, M. *Chem. Commun*. **2003**, 1850. (b) Toma, L. M.; Delgado, F. S.; Ruiz-Pérez, C.; Carrasco, R.; Cano, J.; Lloret, F.; Julve, M. *Dalton Trans.* **2004**, 2836.
(13) Wang, S.; Zuo, J. L.; Gao, S.; Song, Y.; Zhou, H. C.; Zhang, Y. Z.; You, X. Z. *J. Am. Chem. Soc.* **2004**, *126*, 8900.
(14) Ferbinteanu, M.; Miyasaka, H.; Wernsdorfer, W.; Nakata, K.; Sugiura, K. I.; Yamashita, M.; Coulon, C.; Clérac, R. *J. Am. Chem. Soc.* **2005**, *127*, 3090.
(15) (a) Lescouëzec, R.; Lloret, F.; Julve, M.; Vaissermann, J.; Verdaguer, M.; Llusar, R.; Uriel, S. *Inorg. Chem*. **2001**, *40*, 2065. (b) Lescouëzec, R.; Lloret, F.; Julve, M.; Vaissermann, J.; Verdaguer, M. *Inorg. Chem*. **2002**, *41*, 818. (c) Toma, L. M.; Lescouëzec, R.; Toma, L. D.; Lloret, F.; Julve, M.; Vaissermann, J.; Andruh, M. *J. Chem. Soc., Dalton Trans.* **2002**, 3171.
(16) (a) Toma, L.; Lescouëzec, R.; Vaissermann, J.; Delgado, F. S.; Ruiz-Pérez, C.; Carrasco, R.; Cano, J.; Lloret, F.; Julve, M. *Chem. Eur. J.* **2004**, *10*, 6130. (b) Toma, L.; Lescouëzec, R.; Vaissermann, J.; Herson, P.; Marvaud, V.; Lloret, F.; Julve, M. *New J. Chem.* **2005**, *29*, 210.
(17) Toma, L.; Toma, L. M.; Lescouëzec, R.; Armentano, D.; De Munno, G.; Andruh, M.; Cano, J.; Lloret, F.; Julve, M. *Dalton Trans.* **2005**, 1537.

Physical Measurements. Infrared spectra (KBr pellets) were recorded on a Bruker IF S55 spectrometer. Magnetic susceptibility measurements on polycrystalline samples of **1**−**5** were carried out with a Quantum Design SQUID magnetometer in the temperature range 1.9−295 K and under applied magnetic fields of 50 G to 1 T. The magnetization versus magnetic field measurements on the same samples of **1**−**5** were performed at 2.0 K in the field range 0−5 T. The ac measurements on a polycrystalline sample of **3** were performed at frequencies ranging from 0.25 to 1200 Hz with an ac field amplitude of 1 G and no dc field applied. Experimental magnetic data were also corrected for the diamagnetic contribution calculated from Pascal constants. Magnetization measurements on single crystals of **3** were performed by using (i) a magnetometer consisting of several Hall-bars[18] and (ii) an array of micro-SQUIDs[19] on top of which a single crystal of the $Fe^{III}_2Co^{II}$ chain was placed, for higher and lower fields than 1.4 T, respectively. The field can be applied in any direction of the micro-SQUID plane with precision much better than 0.1° by separately driving three orthogonal superconducting coils. The field was aligned with the easy axis of magnetization using the transverse field method.[20] The Hall probes (typically 10 × 10 mm^2) are made of two-dimensional GaAs/GaAsAl heterostructures and work in the temperature range of 1.5−100 K and in magnetic fields of up to 16 T.

Computational Details. All theoretical calculations were carried out with the hybrid B3LYP method,[21−23] as implemented in the GAUSSIAN03 program.[24] Double-ζ quality basis sets, proposed by Ahlrichs and co-workers, have been used for all atoms.[25] The broken symmetry approach has been employed to describe the unrestricted solutions of the antiferromagnetic spin states.[26−29] The geometries of the studied models [**I** and **II** in Figures S14 (top) and S15(a), respectively] were built from the experimental crystal structures. A quadratic convergence method was used to determine the more stable wave functions in the SCF process. The atomic spin densities were obtained from natural bond orbital (NBO) analysis.[30−32]

Crystallographic Data Collection and Structure Determination. Single crystals of compounds **1**−**5** of dimensions 0.30 mm × 0.35 mm × 0.40 (**1**), 0.09 mm × 0.20 mm × 0.27 (**2**), 0.12 mm × 0.15 mm × 0.20 (**3**), 0.01 mm × 0.04 mm × 0.13 (**4**) and 0.11 mm × 0.12 mm × 0.15 mm (**5**) were mounted on Enraf-Nonius CAD-4 (**1**) and Bruker-Nonius KappaCCD (**2**−**5**) diffractometers and used for data collection. Intensity data were collected at 295 (**1**) and 293 K (**2**−**5**) by using graphite monochromated Mo Kα radiation source [$\lambda = 0.71069$ Å (**1**) and 0.71073 Å (**2**−**5**)] with the $\omega - 2\theta$ method. Accurate cell dimensions and orientation matrixes were determined by least-squares refinements of 25 accurately centered reflections with $12 < \theta < 12.3°$ for **1** and through least-squares refinement of the reflections obtained by a $\theta - \chi$ scan (Dirac/lsq method) for **2**−**5**. No significant variations were observed in the intensities of two checked reflections (**2**−**5**) during data collection; for **1**, a decay of 5.52% was observed, and the data were accordingly scaled. Data collection and data reduction for **2-4** were done with the COLLECT[33] and EVALCCD[34] programs. The data were corrected for Lorentz and polarization effects (**1**−**5**). Empirical absorption corrections were performed by the use of *DIFABS*[35] (**1**) and *SADABS*[36] (**2**−**5**). The indexes of data collection were $0 \le h \le 40$, $0 \le k \le 16$, $-37 \le l \le 32$ for **1**, $-9 \le h \le 9$, $-15 \le k \le 14$, $-17 \le l \le 17$ for **2**, $-9 \le h \le 8$, $-13 \le k \le 10$, $-16 \le l \le 14$ for **3**, $-9 \le h \le 9$, $-15 \le k \le 15$, $-16 \le l \le 17$ for **4**, and $-10 \le h \le 10$, $-15 \le k \le 15$, $-11 \le l \le 17$ for **5**. Of the 11472 (**1**), 5030 (**2**), 3984 (**3**), 4964 (**4**), and 4941 (**5**) measured independent reflections in the θ range 1.0−25.0° (**1**), 4.10−30.0° (**2**), 3.21−27.50° (**3**), 4.01−29.99° (**4**) and 5.03−30.00° (**5**), 6213 (**1**), 3744 (**2**), 2521 (**3**), 2538 (**4**), and 3499 (**5**) were considered as observed [$I \ge 1.5\sigma(I)$ (**1**) and $I \ge 2\sigma(I)$ (**2**−**5**)] and used for the refinement of the structures. The structure of **1** was solved by direct methods through SHELX-86[37] and subsequently refined by Fourier recycling. The final full-matrix least-squares refinement on F for **1** was done by the PC version of CRYSTALS.[38] All calculations for data reduction, structure solution, and refinement for **2**−**5** were done by standard procedures.[39] The structures of **2**−**5** were also solved by direct methods and refined with full-matrix least-squares technique on F^2 using the SHELXS-97 and SHELXL-97 programs.[40] All non-hydrogen atoms in **1**−**5** were refined anisotropically. The hydrogen atoms of the water molecules (**1**−**5**) were not found, whereas those of the bpym ligand (**1**−**5**) and the PPh_4^+ cation (**1**) were placed in calculated positions. The hydrogen atoms were refined with isotropic temperature factors for all compounds. The final geometrical calculations and the graphical manipulations for **1**−**5** were carried out with PARST95[41] and CRYSTALMAKER[42] programs, respectively. The crystal data and details of the structure refinements of **1**−**5** are summarized in Table S1. Selected bond distances and angles are listed in Tables S2 (**1**), S3 (**2**, **3**, and **5**), and S4 (**4**).

Results and Discussion

Synthesis. Cyanide and bpym are well-known ligands in magnetic studies because of their remarkable ability to mediate strong magnetic interactions between the paramagetic centers which are bridged by them.[43,44] The coexistence of the two ligands in the stable mononuclear low-spin iron(III) complex $[Fe(bpym)(CN)_4]^-$ makes this species a very appealing candidate to build extended magnetic systems. In the present work, we show for the first time how the use of the heteroleptic $[Fe(bpym)(CN)_4]^-$ complex as a ligand toward fully solvated divalent first-row transition metal ions [M = Zn (**2**), Co (**3**),

(18) Sorace, L.; Wernsdorfer, W.; Thirion, C.; Barra, A. L.Pacchioni, M.; Mailly, D.; Barbara, B. *Phys. Rev. B* **2003**, *68*, 220407(R).
(19) Wernsdorfer, W. *Adv. Chem. Phys.* **2001**, *118*, 99.
(20) Wernsdorfer, W.; Chakov, N. E.; Christou, G. *Phys. Rev.* **2004**, *B70*, 132413.
(21) Becke, A. D. *Phys. Rev. A* **1988**, *38*, 3098.
(22) Lee, C.; Yang, W.; Parr, R. G. *Phys. Rev. B* **1988**, *37*, 785.
(23) Becke, A. D. *J. Chem. Phys.* **1993**, *98*, 5648.
(24) Frisch, M. J.; et al. *GAUSSIAN 03*, Revision C.03; Gaussian, Inc.: Wallingford, CT, 2004.
(25) Schaefer, A.; Horn, A.; Ahlrichs, R. *J. Chem. Phys.* **1992**, *97*, 2571.
(26) Cano, J.; Alemany, P.; Alvarez, S.; Verdaguer, M.; Ruiz, E. *Chem. Eur. J.* **1998**, *4*, 476.
(27) Ruiz, E.; Cano, J.; Alvarez, S.; Alemany, P. *J. Am. Chem. Soc.* **1998**, *120*, 11122.
(28) Ruiz, E.; Cano, J.; Alvarez, S.; Alemany, P. *J. Comput. Chem.* **1999**, *20*, 1391.
(29) Cano, J.; Ruiz, E.; Alemany, P.; Lloret, F.; Alvarez, S. *J. Chem. Soc., Dalton Trans.* **1999**, 1669.
(30) Carpenter, J. E.; Weinhold, F. *J. Mol. Struct.* **1988**, *169*, 41.
(31) Reed, A. E.; Curtis, L. A.; Weinhold, F. *Chem. Rev.* **1988**, *88*, 899.
(32) Weinhold, F.; Carpenter, J. E. *The Structure of Small Molecules and Ions*; Plenum: Nw York,1988; p 227.
(33) Hooft, R. W. W. *COLLECT*; Nonius BV: Delft, The Netherlands, 1999.
(34) Duisenberg, A. J. M.; Kroon-Batenburg, L. M. J.; Schreurs, A. M. M. *J. Appl. Crystallogr.* **2003**, *36* 220 (*EVALCCD*).
(35) Walker, N.; Stuart, D. *Acta Crystallogr.* **1983**, *A39*, 156.
(36) *SADABS Empirical Absorption Program*, version 2.03; Bruker AXS Inc.: Madison, WI, 2000.
(37) Sheldrick, G. M. *SHELX-86: Program for Crystal Structure Solution*; University of Göttingen: Göttingen, Germany, 1996.
(38) Watkin, D. J.; Prout, C. K.; Carruthers, J. R.; Betheridge, P. W. *CRYSTALS*; Chemical Crystallography Laboratory, University of Oxford: Oxford, United Kingdom, 1996, Issue 10.
(39) Farrugia, L. J. (*WING*) *J. Appl. Crystallogr.* **1999**, *32*, 837.
(40) Sheldrick, G. M. *SHELX-97: Programs for Crystal Structure Analysis*, Release 97-2; Institüt für Anorganische Chemie der Universität: Göttingen, Germany, 1998.
(41) Nardelli, M. *PARST95*, *J. Appl. Crystallogr.* **1995**, *28*, 659.
(42) *CrystalMaker*, 4.2.1; CrystalMaker Software: Bicester, Oxfordshire X26 3TA, UK.
(43) (a) Verdaguer, M.; Bleuzen, A.; Marvaud, V.; Vaissermann, J.; Seuleiman, M.; Desplanches, C.; Scuiller, A.; Train, C.; Garde, R.; Gelly, G.; Lomenech, C.; Rosenman, I,; Veillet, R.; Cartier, C.; Villain, F. *Coord. Chem. Rev.* **1999**, *190*−*192*, 103 and refereces therein. (b) Ohba, M.; Okawa, H. *Coord. Chem. Rev.* **2000**, *198*, 313 and references therein.
(44) (a) De Munno, G.; Julve, M. In *Metal Ligand Interactions. Structure and Reactivity*; Russo, N., Salahub, D. R., Eds.; NATO Advanced Study Institute Series 474; Kluwer: Dordrecht, 1996; p 139 and references therein. (b) De Munno, G.; Lloret, F.; Julve, M. In *Magnetism: A Supramolecular Function*; Kahn, O., Ed.; NATO Advanced Study Institute Series 484; Kluwer: Dordrecht, 1996; p 555 and references therein. (c) Vangdal, B.; Carranza, J.; Lloret, F.; Julve, M.; Sletten, J. *Dalton Trans.* **2002**, 566.

Cu (**4**), and Mn (**5**)] affords the neutral 4,2-ribbonlike bimetallic chains of formula $\{[Fe^{III}(bpym)(CN_4)]_2M^{II}(H_2O)_2\}\cdot 6H_2O$. The $[Fe(bpym)(CN)_4]^-$ unit acts as a bis-monodentate ligand through two cis cyano groups.

This coordination mode as well as the monodentate (across one of the four cyano groups) and tris-monodentate ones (three of the four cyano groups being involved) was previously observed in the parent low-spin iron(III) $[Fe(bipy)(CN)_4]^-$ (bipy = 2,2′-bipyridine) and $Fe(phen)(CN)_4]^-$ (phen = 1,10-phenanthroline) units leading to heterobimetallic trinuclear[15b] and tetranuclear[15c,17] compounds and single[5,12b,15a] and double[12b,15b] 4,2-ribbonlike chains. These studies evidenced the relevance of the solvent in the formation of the double 4,2-ribbonlike chains. These double chains can be viewed as the condensation of two single 4,2-ribbonlike chains by the substitution of an axially coordinated water molecule at M by a cyanide-nitrogen atom. In light of these results and keeping in mind the additional coordination possibilities offered by the presence of terminal bpym in the complex $[Fe(bpym)(CN)_4]^-$, its use as a ligand toward either fully solvated metal ions or partially blocked complexes would provide us with a plethora of new heterometallic magnetic species in the very near future.

Description of the Structures. $PPh_4[Fe^{III}(bpym)(CN)_4]\cdot H_2O$ (1). The crystallographic analysis of **1** shows that its structure consists of mononuclear $[Fe(bpym)(CN)_4]^-$ anions (Figure S1), tetraphenylphosphonium cations, and water molecules of crystallization which are linked by electrostatic forces, hydrogen bonds, and van der Waals interactions.

Two crystallographically independent iron atoms [Fe(1) and Fe(2)] occur in **1**, and they are coordinated to two bpym-nitrogen atoms and four cyanide-carbon atoms, taking distorted octahedral geometries. The short bite of the bidentate bpym ligand [80.9(2) and 80.5(2)° at Fe(1) and Fe(2), respectively] is at the origin of this distortion from the ideal geometry. The values of the Fe−N(bpym) bonds in **1** are comprised of those between the low-spin iron(II) unit $[Fe(bpym)_3]^{2+}$ in the compounds $[Fe(bpym)_3](ClO_4)_2$ [average value 1.970(5) Å][45] and $Fe(bpym)_3Na(H_2O)_2Fe(ox)_3\cdot 4H_2O$ (ox = oxalate) [av value 1.978(4) Å][46] and those of the high-spin iron(III) complex $[Fe(bpym)Cl_3(H_2O)]\cdot H_2O$ [mean value 2.207(3) Å],[47] but they are the same as those found in the low-spin iron(III) complexes $PPh_4[Fe(bipy)(CN)_4]\cdot H_2O$ [1.98(2) and 2.00(2) Å][15b] and $K[Fe(bipy)(CN)_4]\cdot H_2O$ [1.991(3) and 1.990(3) Å].[15c] This agreement is also observed between the values of the Fe−C(cyano) bond lengths of **1** [1.915(5)−1.949(6) Å at Fe(1) and 1.910(5)−1.954(5) Å at Fe(2)] and those reported for other cyano-containing mononuclear low-spin iron(III) complexes [1.87(2)−1.95(1) Å].[15,48] The presence of the tetraphenylphosphonium cation in the structure of **1** and the magnetic behavior of this compound demonstrate that it is a low-spin iron(III) complex. Additional support of this low-spin iron(III) character of **1** comes from the values of the higher frequency cyanide stretching in its infrared spectrum [doublet at 2124m and 2112m cm^{-1}] which compare very well with those observed in $PPh_4[Fe(bipy)(CN)_4]\cdot H_2O$ [2118m cm^{-1}][15b] and $K[Fe(bipy)(CN)_4]\cdot H_2O$ [2134s and 2114w cm^{-1}].[15c] The two types of $[Fe(bpym)(CN)_4]^-$ anions are grouped by pairs through hydrogen bonds involving the crystallization water molecules O(1) and O(2) and the terminal cyanide nitrogens (Figure S2).

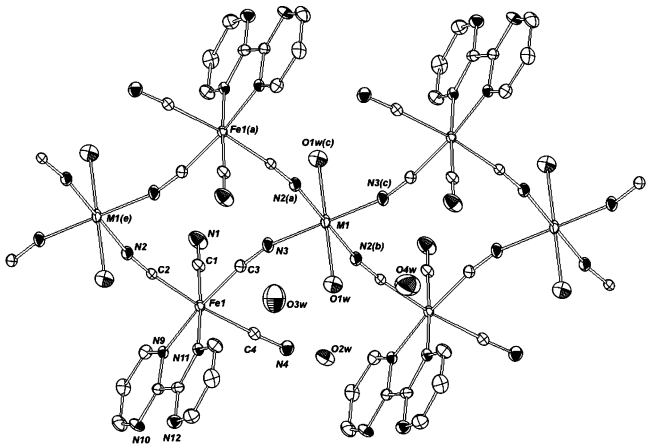

Figure 1. Perspective view of a fragment of the 4,2-ribbonlike bimetallic chain of **2** (M = Zn), **3** (M = Co), **4** (M = Cu), and **5** (M = Mn) running parallel to the *a* axis. The hydrogen atoms have been omitted for clarity. Symmetry code: (a) = $-x$, $1-y$, $1-z$; (b) = $1+x$, y, z; (c) = $1-x$, $1-y$, $1-z$; (e) = $-1+x$, y, z.

The bpym ligands are practically planar, but they are clearly distorted because of their bidentate coordination (see end of Table S2). The value of inter-ring carbon−carbon bond length of the bpym ligands [1.497(8) and 1.472(8) Å for C(15)−C(16) and C(25)−C(26), respectively] is very close to that found in the free molecule in the solid state [1.502(4) and 1.497(1) Å].[49] The triatomic Fe−C−N set of atoms at each cyanide are almost linear. The values of the cyanide C−N bonds agree with those reported for other cyano-containing mononuclear low-spin iron(III) complexes.[15,48,50] The tetraphenylphosphonium cations exhibit the expected tetrahedral shape, and their bond distances and angles are as expected.

$\{[Fe^{III}(bpym)(CN_4)]_2M^{II}(H_2O)_2\}\cdot 6H_2O$ [M = Zn (2), Co (3), and Mn (5)]. **2**, **3**, and **5** are isostructural compounds whose structures are made up of neutral cyanide-bridged 4,2-ribbonlike bimetallic chains of formula $\{[Fe^{III}(bpym)(CN_4)]_2M^{II}(H_2O)_2\}$ [M = Zn (**2**), Co (**3**), and Mn (**5**)] with run parallel to the *a* axis (Figure 1). These chains are stacked along the *b* axis through hydrogen bonds (see end of Table S3) involving discrete centrosymmetric water hexameric rings with two dangling water molecules in trans positions [Figure 2 (top)] to form a layered structure (Figure S3). These rings adopt an icelike chair conformation.[51,52]

The iron and M atoms in **2**, **3**, and **5** are six-coordinated: two nitrogen atoms from bpym and four cyanide-carbon atoms around the iron center and two water molecules in trans positions and four cyanide-nitrogen atoms around the M atom build distorted octahedral geometries. The bond distances and angles around the iron atom in the $[Fe(bpym)(CN)_4]^-$ unit in **2**, **3**, and **5** agree with those observed for this entity in **1**. The M−O(w1) bond lengths are close to those observed in the related $\{[Fe^{III}(bipy)(CN)_4]_2M^{II}(H_2O)_4\}\cdot 4H_2O$ (M = Mn and Zn) trinuclear

(45) De Munno, G.; Julve, M.; Real, J. A. *Inorg. Chim. Acta* **1997**, *255*, 185.
(46) Armentano, D.; De Munno, G.; Faus, J.; Lloret, F.; Julve, M. *Inorg. Chem.* **2001**, *40*, 655.
(47) De Munno, G.; Ventura, W.; Viau, G.; Lloret, F.; Faus, J.; Julve, M. *Inorg. Chem.* **1998**, *37*, 1458.
(48) Lu, T. H.; Kao, H. Y.; Wu, D. I.; Kong, K. C., Cheng, C. H. *Acta Crystallogr., Sect. C* **1988**, *44*, 1184.
(49) Fernholt, L.; Rømming, C.; Sandal, S. *Acta Chem. Scand., Ser. A* **1981**, *35*, 707.
(50) Vannerberg, N. G. *Acta Chem. Scand.* **1972**, *26*, 2863.
(51) Eisenberg, D.; Kauzmann, W. *The Structure and Properties of Water*; Oxford University Press: Oxford, 1969.
(52) Narten, A. H.; Thiessen, E.; Blum, L. *Science* **1982**, *217*, 1033.

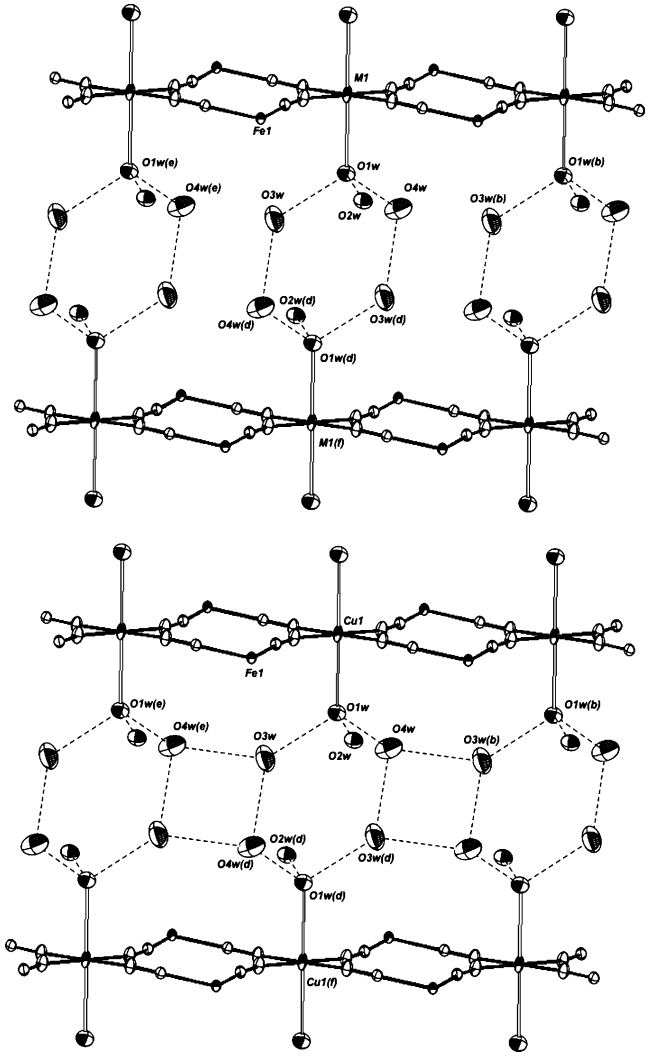

Figure 2. Perspective views of the stacking of two fragments of neighboring chains of **2** (M = Zn), **3** (M = Co), and **5** (M = Mn) (top) and **4** (M = Cu) (bottom) showing the interchain linking through hydrogen bonds. The bpym molecules and terminal cyanide ligands have been omitted for clarity. Symmetry code: (b) = 1+*x*, *y*, *z*; (d) = 1−*x*, −*y*, 1−*z*; (f) = *x*, −1+*y*, *z*.

species[15b] and $\{[Fe^{III}(phen)(CN)_4]_2Mn^{II}(H_2O)_4\}\cdot 4H_2O$ and $\{[Fe^{III}(L)(CN)_4]_2Co^{II}(H_2O)_2\}\cdot 4H_2O$ (L = bipy and phen) 4,2-ribbonlike chains.[5,15a] The M(1)-N−C angle for the bridging cyanide ligands is largely bent. The C−N bond lengths for terminal cyanide groups in **2**, **3**, and **5** compare well with those observed in **1** and they are very close to those of the bridging cyanide ligands. The CN stretching region of the IR spectrum of **2**, **3**, and **5** is consistent with the occurrence of bridging [medium intensity peaks at 2174 (**2**), 2171 (**3**), and 2157 cm^{-1} (**5**)] and terminal [weak intensity peaks at 2124 and 2114 (**2**), 2126 and 2113 (**3**), and 2132 cm^{-1} (**5**)] cyanide ligands.

The bpym ligand as a whole is quasi-planar, and the value of the inter-ring carbon−carbon bond distance [1.486(3) (**2**), 1.470(6) (**3**), and 1.473(3) Å (**5**)] is very close to that observed in **1**. No significant graphite-like interaction between bpym molecules of adjacent chains occur in **2**, **3**, and **5**. The intrachain Fe(1)···M(1) separations through bridging cyanide are 4.9904(5) (**2**), 4.9970(6) (**3**), and 5.0398(5) Å (**5**) [Fe(1)···M(1)] and 5.0532(5) (**2**), 5.0521(6) (**3**), and 5.0908(5) Å (**5**) [Fe(1)··· M(1e)], values which are much shorter than the metal−metal separation through the water clusters [10.7418(5) (**2**), 10.7244(5) (**3**), 10.7429(9) Å (**5**) for M(1)···M(1f)].

$\{[Fe^{III}(bpym)(CN_4)]_2Cu^{II}(H_2O)_2\cdot 6H_2O$ (4). The structure of **4** consists of cyanide-bridged crossed $Fe^{III}-Cu^{II}$ zigzag chains of formula $\{[Fe^{III}(bpym)(CN_4)]_2Cu^{II}(H_2O)_2\}$ which run also parallel to the *a* axis as in **2**, **3**, and **5** (Figure 1), the main difference being the occurrence in **4** of fused four- and five-membered water rings [Figure 2 (bottom)] linking the neutral chains through hydrogen bonds (see end of Table S4) to afford a layered structure (Figure S4). The hexameric ring in **4** exhibits also the chairlike conformation.

As in **2**, **3**, and **5**, the $[Fe(bpym)(CN)_4]^-$ unit in **4** acts as a bis-monodentate bridging ligand toward two trans diaquacopper(II) entities through two of its four cyanide groups in cis positions affording a 4,2-ribbonlike bimetallic chain. Each iron atom in **4** is six-coordinated, two bpym-nitrogen and four cyanide-carbon atoms forming a distorted octahedral geometry. The values of the bond lengths at the iron atom and that of the angle subtended by the bidentate bpym agree with those reported for **2**, **3**, and **5**. Each copper atom lies on an inversion center, and it has a distorted, elongated octahedral coordination geometry: four cyanide-nitrogen atoms build the equatorial plane, and two water molecules fill the axial positions. This situation around the copper atom contrasts with that observed in the related 4,2-ribbonlike chain of formula $\{[Fe^{III}(phen)(CN_4)]_2Cu^{II}(H_2O)_2\}\cdot 4H_2O$ where the two trans coordinated water molecules and two cyanide-nitrogen atoms define the equatorial positions, whereas the axial ones are filled by other two cyanide-nitrogen atoms.[12b] The Fe−C−N angles for both terminal and bridging cyanide ligands depart somewhat from the strict linearity, whereas those of the Cu−C−N units are significantly bent. The occurrence of both terminal and bridging cyanide ligands in **4** is suggested by the presence of two stretching vibrations at 2186m (bridging) and 2117w (terminal) in its IR spectrum.

The heterocyclic bpym ligand is quasi-planar, and no significant $\pi-\pi$ interactions between bpym ligands are observed. The intrachain iron···copper separations through bridging cyanide in **4** are 4.9268(7) [Fe(1)···M(1)] and 5.0009(8) Å [Fe(1)···M(1e)], values which are much shorter than the metal−metal separation through the water cluster [10.8763(8) Å for Cu(1)···Cu(1f)].

Magnetic Properties of 1, 2, 4, and 5. The magnetic properties of complexes **1** and **2** are shown in Figure S5 under the form of $\chi_M T$ versus *T* plot [χ_M is the magnetic susceptibility per mole of iron(III)]. The values of $\chi_M T$ at 300 K are 0.615 (**1**) and 0.644 (**2**) $cm^3\ mol^{-1}$ K. Both $\chi_M T$ versus *T* plots decrease quasi-linearly when cooling, and they reach values of 0.46 (**1**) and 0.455 (**2**) $cm^3\ mol^{-1}$ K at 1.9 K. This is the expected behavior for a magnetically isolated distorted low-spin octahedral iron(III) system with spin−orbit coupling of the $^2T_{2g}$ ground term. The similarity between the magnetic behavior of **2** (4,2-ribbonlike bimetallic chain) and complex **1** shows that the magnetic coupling between iron(III) centers separated by more than 10 Å through the diamagnetic −CN−Zn−CN− bridging skeleton in **2** must be very small, as expected. At this respect, it deserves to be noted that a weak magnetic coupling of $J = -1.3\ cm^{-1}$ [the Hamiltonian being defined as $\hat{H} = -J\hat{S}_{Fe(1)}\cdot\hat{S}_{Fe(2)}$] was roughly estimated in the centrosymmetric trinuclear complex $\{[Fe^{III}(bipy)(CN)_4]_2Zn^{II}(H_2O)_4\}\cdot 4H_2O$.[15b]

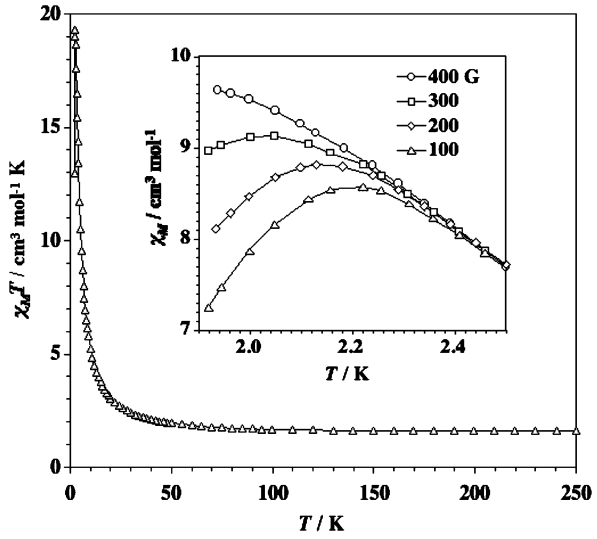

Figure 3. Thermal dependence of the $\chi_M T$ product for complex **4** under an applied magnetic field of 100 G: (△) experimental data; (–) eye guideline. (Inset) Field dependence of the magnetic susceptibility of **4** at very low temperatures (the applied magnetic field varying in the range 100–400 G).

For a low-spin iron(III) ion in O_h symmetry, the $^2T_{2g}$ term is split under a rhombic distortion (C_{2v} symmetry) into a singlet ground state ($^2A_1$) and two excited doublets ($^2B_1 + {}^2B_2$) which are separated by an average energy gap (Δ). Consequently, the magnetic data of **1** and **2** were analyzed through the Hamiltonian of eq 1

$$\hat{H} = -\kappa\lambda\hat{L}\hat{S} + \Delta[\hat{L}_z{}^2 - 2/3] + \beta H[-\kappa\hat{L} + 2\hat{S}] \qquad (1)$$

The spin–orbit coupling (first term), an axial distortion (second term), and the Zeeman effect (last term) are considered in this Hamiltonian, and we used $L = 1$ due to the isomorphism between the T_2 and P terms ($[T_2] = -[P]$).[53] In this Hamiltonian, λ is the spin–orbit coupling, κ is the orbital reduction factor, and Δ is the energy gap between the A_1 singlet and the $E(B_1 + B_2)$ doublet. Best-fit parameters are $\lambda = -362$ cm^{-1}, $\Delta = 680$ cm^{-1}, $\kappa = 0.87$, and $R = 2.2 \times 10^{-6}$ for **1** and $\lambda = -336$ cm^{-1}, $\Delta = 578$ cm^{-1}, $\kappa = 0.90$, and $R = 1.1 \times 10^{-6}$ for **2** where R is the agreement factor defined as $\sum_j[(\chi_M T)_{obsv}{}^j - (\chi_M T)_{calc}{}^j]^2/\sum_j[(\chi_M T)_{obsv}{}^j]^2$).

The temperature dependence of the $\chi_M T$ product for **4** per $Fe^{III}{}_2Cu^{II}$ unit is shown in Figure 3. $\chi_M T$ at room temperature is 1.61 cm^3 mol^{-1} K, a value which is as expected for one copper(II) and two low-spin iron(III) ions magnetically isolated. Upon cooling, $\chi_M T$ increases continuously in agreement with an intrachain ferromagnetic coupling between the spin doublets of the copper(II) and low-spin iron(III) centers. The increase is smooth in the high-temperature range and sharp at $T < 50$ K. $\chi_M T$ reaches a maximum value of 19.50 cm^3 mol^{-1} K at 2.5 K and further decreases to 13.0 cm^3 mol^{-1} K at 1.9 K under an applied magnetic field of $H = 100$ G. The magnetic susceptibility of **4** is field dependent for $T < 2.5$ K (see inset of Figure 3). A maximum of susceptibility occurs at 2.2 K for $H = 100$ G, revealing the occurrence of a weak antiferromagnetic interaction between the ferromagnetic bimetallic chains in **4**. This maximum is shifted toward lower temperatures when increasing the applied magnetic field, and it disappears for $H \geq 400$ G, suggesting a field-induced transition from an antiferromagnetic to a ferromagnetic ground state. This magnetic behavior of **4** is consistent with its crystal structure: parallel $Fe^{III}{}_2Cu^{II}$ ferromagnetic chains with interchain antiferromagnetic coupling. The magnetization at saturation (M_S) tends to a value of 3.0 μ_B (Figure S5), as expected for a ferromagnetically coupled $Fe^{III}{}_2Cu^{II}$ unit with $S_{Fe} = S_{Cu} = {}^1/_2$. The sigmoidal shape of the magnetization (M) versus H plot at 2.0 K (inset of Figure S6) with an inflection point at 400 G gives the order of magnitude of the interchain magnetic interaction, ca. 0.04 cm^{-1}. No alternating current (ac) signals were observed for **4** down to 1.9 K at $H = 0$ G. The lack of SCM behavior in **4** in the investigated range of temperatures, [in contrast to what is observed for **3** (see below)], is most likely due to the lower anisotropy of the copper(II) ion compared to that of the high-spin cobalt(II). The lack of an exact model to analyze the magnetic data of the ferromagnetic chain **4** with two intrachain ferromagnetic interactions moved us to use the Monte Carlo methodology to simulate the magnetic data and determine the magnitude of the intrachain magnetic couplings. A value of $J_{Fe-Cu} = +20.9$ cm^{-1} was obtained for **4** (see below). DFT-type calculations were also performed on a model fragment of **4** to analyze the exchange pathway and to check the computed value of the exchange interaction obtained through the Monte Carlo methodology (see below).

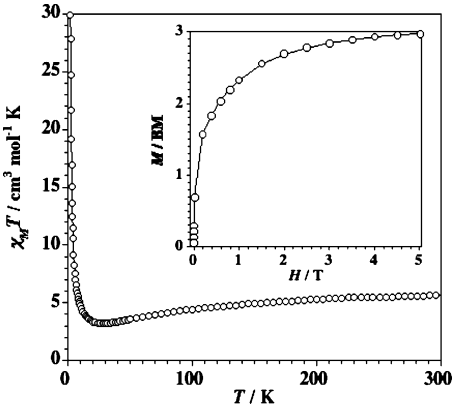

Figure 4. Thermal dependence of the $\chi_M T$ product for complex **5**: (○) experimental data; (–) eye guideline. (Inset) Magnetization versus H plot at 2.0 K.

The temperature dependence of the $\chi_M T$ product for **5** per $Fe^{III}{}_2Mn^{II}$ unit is shown in Figure 4. $\chi_M T$ at room temperature is 5.64 cm^3 mol^{-1} K, a value which is as expected for a high-spin manganese(II) and two low-spin iron(III) ions magnetically isolated. As the temperature is lowered, $\chi_M T$ smoothly decreases, exhibits a minimum at ca. 25 K ($\chi_M T$ being 3.22 cm^3 mol^{-1} K), and increases sharply to reach a value of 30.0 cm^3 mol^{-1} K at 1.9 K. The magnetization curve for 5 at 2.0 K is shown in the inset of Figure 4. A value of 3.0 μ_B is attained at 5 T (the maximum available magnetic field in our device). The features observed in Figure 4 are as expected for a ferrimagnetic behavior:[54] the noncompensation between the antiferromagnetically coupled Mn(II) spin sextet and Fe(III) spin doublet across the cyanide bridges in **5** accounts for this well-documented magnetic behavior. As done for **4**, the successful modelization

(53) Herrera, J. M.; Bleuzen, A.; Dromzée, Y.; Julve, M.; Lloret, F.; Verdaguer, M. *Inorg. Chem.* **2003**, *42*, 7052.

(54) (a) Verdaguer, M.; Julve, M.; Michalowicz, A.; Kahn, O. *Inorg. Chem.* **1983**, *19*, 2624. (b) Verdaguer, M.; Gleizes, A.; Renard, J. P.; Seiden, J. *Phys. Rev. B* **1984**, *29*, 5144. (c) Lloret, F.; Julve, M.; Ruiz, R.; Journaux, Y.; Nakatani, K.; Kahn, O.; Sletten, J. *Inorg Chem.* **1993**, *32*, 27.

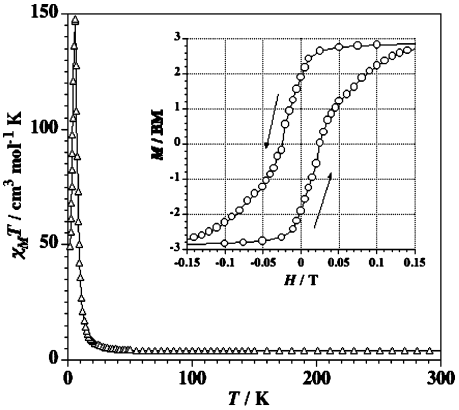

Figure 5. Thermal dependence of the $\chi_M T$ product for complex **3** under an applied magnetic field of 100 G: (Δ) experimental data; (–) eye guideline. (Inset) Hysteresis loop for **3** at 2.0 K.

of the magnetic data of **5** through Monte Carlo methodology allowed us to estimate a value of the magnetic coupling J_{Fe-Mn} of -10.8 cm^{-1} which was also substantiated by DFT type calculations (see below).

Single-Chain Magnet Behavior in 3. The temperature dependence of the $\chi_M T$ product for **3** per $Fe^{III}_2Co^{II}$ unit is shown in Figure 5. At room temperature, the $\chi_M T$ product of a polycrystalline sample of **3** per $Fe^{III}_2Co^{II}$ unit is 4.0 cm^3 mol^{-1} K and it corresponds to the presence of one high-spin cobalt(II) ($S_{Co} = {}^3/_2$) and two low-spin iron(III) ($S_{Fe} = {}^1/_2$) ions. Upon cooling, $\chi_M T$ increases continuously in agreement with an intrachain ferromagnetic interaction between Co^{II} and Fe^{III} centers. The increase is smooth in the high-temperature range and sharp at $T < 40$ K. $\chi_M T$ reaches a maximum value of 148 cm^3 mol^{-1} K at 5.7 K ($H = 100$ G) and further decreases linearly with T (as the magnetization becomes field-dependent) to a value of ca. 50 cm^3 mol^{-1} K at 1.9 K. The magnetization versus H plot at 2.0 K exhibits an abrupt increase at very low fields, and it reaches a value of 3.7 μ_B at 5 T (the maximum available magnetic field in our device). A hysteresis loop is observed for **3** at 2.0 K (see inset of Figure 5) with values of the coercive field (H_c) and remnant magnetization (M_r) of 250 G and 2.0 BM, respectively.

The hysteresis loops were studied in detail with the micro-SQUID technique.[19] A single crystal of **3** was attached on the micro-SQUID array using Apiezon grease. The field was aligned with the easy axis of magnetization using the transverse field method.[20] Typical hysteresis loops are presented in Figures 6 and S7. The chain **3** displays smooth hysteresis loops which are strongly temperature- and field sweep rate-dependent. A detailed study of the temperature and field sweep rate dependences of the coercive fields are presented below. No hysteresis is observed in the magnetization plot at 3.2 K as shown in Figure S8. A double-S magnetization curve occurs at small magnetic field loops establishing weak antiferromagnetic interchain interactions. The field derivative of the magnetization curve (inset of Figure S8) allow us to obtain the interaction field of 0.016 T.

The slow relaxation of the magnetization of **3** was studied at higher temperatures with ac magnetic susceptibility. A frequency-dependent out-of-phase component (χ'') was observed below 6.4 K (Figure 7a). The maximum of χ'' can be used to get the mean relaxation (τ). The fact that the maximum of χ'' decreases with decreasing frequency confirms the small interchain coupling. At lower temperatures the relaxation rate becomes too slow for ac magnetic susceptibility measurements, and we used dc relaxation measurements to extract the relaxation time. At a given temperature, the magnetization was first saturated in a high magnetic field. After sweeping the field down to zero with a field sweep rate of 0.14 T/s, the magnetization decay was measured as a function of time (Figure S9). Because the decay is not exponential, we used a scaling procedure to obtain the mean relaxation time (τ). The ac and dc relaxation times are plotted into an Arrhenius plot [$\tau = \tau_o \exp(E_a/kT)$, τ_o being the preexponential factor and E_a the effective energy barrier for spin reversal]. Two regimes are observed in Figure 7 b: (i) above 3.0 K, the thermal dependence of the relaxation time follows

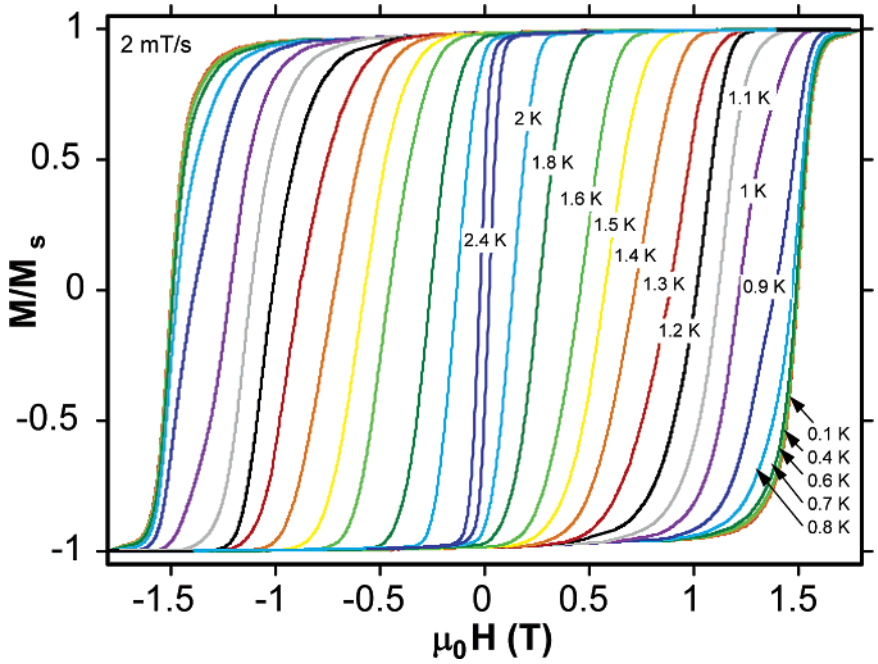

Figure 6. Hysteresis loops for a single crystal of **3** at several temperatures and 0.002 T/s. The field is aligned with the easy axis of magnetization.

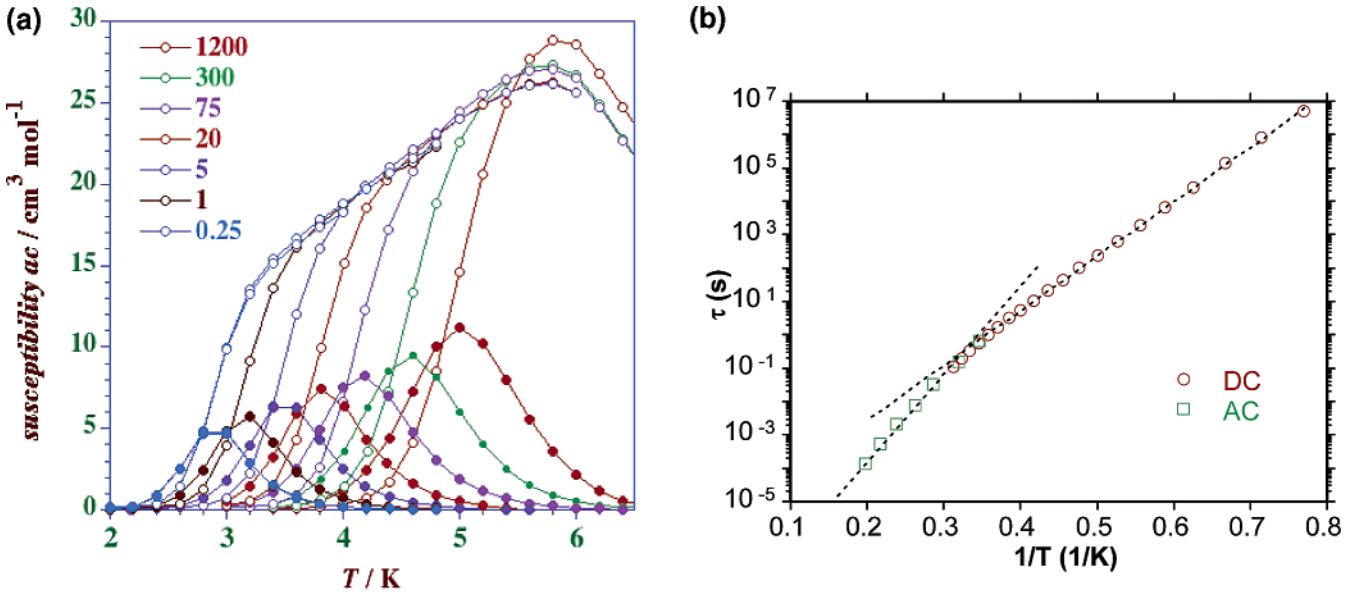

Figure 7. (a) In-phase (open circles) and out-of-phase (filled circles) components of the ac susceptibility of **3** at $T < 6.4$ K in a 1 G field oscillating at different frequencies (0.25−1200 Hz) without dc magnetic field. (b) Plot of ln τ against $1/T$ for **3**: squares are experimental data from ac susceptibility measurements and circles are from dc decay measurements. The dotted lines are least-squares fits to the Arrhenius law (see text).

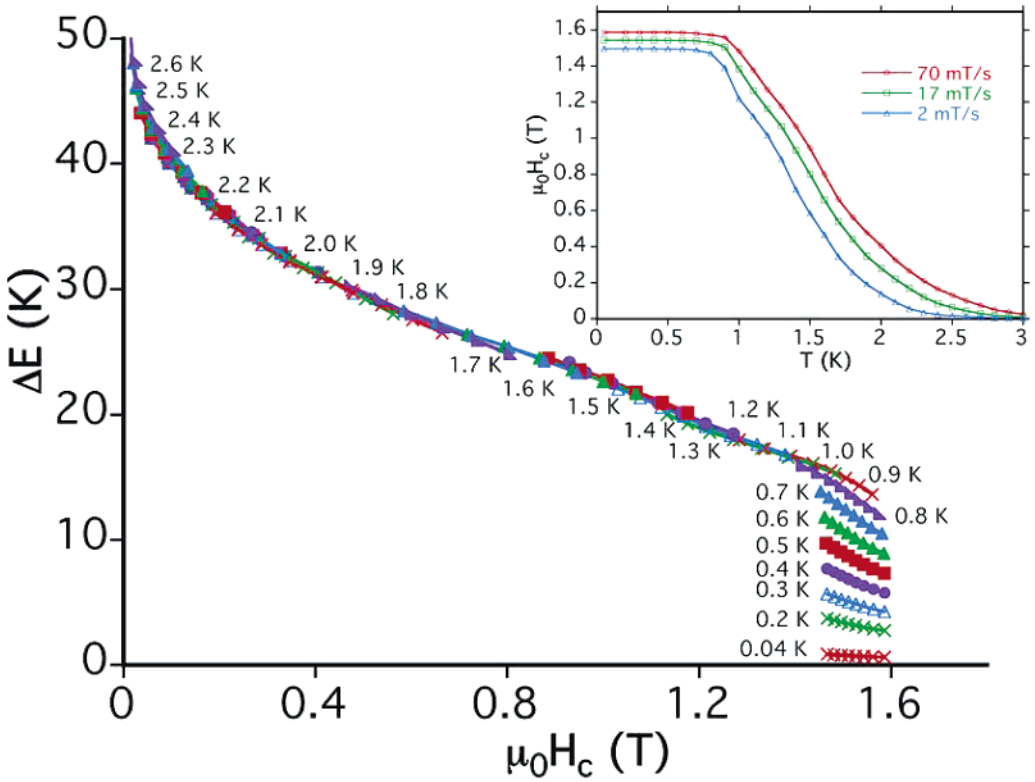

Figure 8. Field dependence of the energy barrier of the chain **3** obtained from eq 2 and the set of H_c (T,v) data from Figure S11. (Inset) Coercive field H_c for the chain **3** as a function of the temperature.

an Arrhenius law with an activation energy of $E_a/k = 61.4$ K and $\tau_o = 7.9 \times 10^{-10}$ s; (ii) below 3 K, a departure from this simple behavior was observed, and a smaller activation energy of 37.8 K and $\tau_o = 1.5 \times 10^{-9}$ s are found. We interpret the crossover at about 3 K as the manifestation of finite-size effects.[55] Indeed, it has been predicted that the activation energy of the relaxation time should decrease from $(4J + D)S^2$ to $(2J + D)S^2$ at the temperature where the correlation length equals the chain length.[55] In our case, a direct application of the model is not possible because of a more complicated coupling scheme of the spins and the strong spin−orbit coupling of the cobalt centers. However, this interpretation is reasonable because the correlation length becomes extremely long at low temperature. The occurrence of a very small number of defects is therefore limiting the correlation lengths.

The relaxation rate at $H = 0$ is extremely small below 1.3 K. We applied therefore a magnetic field to study the low-temperature relaxation process. The temperature and field sweep rate dependences of the coercive fields (H_c) were measured, and they are plotted in the inset of Figure 8 and in Figure S10.

As expected for a thermally activated process, the values of H_c increase with the decreasing temperature T and increasing field sweep rate $\upsilon = dH/dt$. Furthermore, all our measurements showed an almost logarithmic dependence of H_c on the field sweep rate (Figure S10). H_c becomes temperature independent below ca. 0.8 K.

We analyzed the set of $H_c(T,\upsilon)$ data with a model of thermally activated nucleation of magnetization reversal analogous to that of a magnetic single-domain particle. The model was recently applied to SMMs[56] and SCMs[57] and allowed a detailed understanding of the reversal mechanism. Whereas the magnetization relaxation is described at high temperature by the Glauber model, the relaxation at $H = 0$ at low temperature (below 1.3 K) is extremely small. We applied therefore a magnetic field to drive the relaxation at the low temperatures, that is the anisotropy barrier can be lowered by applying a magnetic field in the opposite direction to that of the chain magnetization. When the applied field is close enough to the nucleation field of a domain wall, thermal fluctuations are sufficient to allow the system to overcome the nucleation barrier, and a domain wall nucleates. Then, due to the applied field, the magnetization of the entire chain reverses via a domain wall propagation process. The domain wall nucleation can be thermally activated at high temperatures or driven by quantum tunneling at low temperatures.[58−61]

This stochastic nucleation process can be studied via the magnetization decay when ramping the applied field at a given rate and measuring the coercive field H_c which corresponds to the mean nucleation field of a domain wall. H_c is then measured as a function of the field sweep rate and temperature (inset of Figure 8 and Figure S10). The coercive field of an assembly of identical noninteracting SCMs is given by eq 2

$$H_c(T,\upsilon) = H_c^0\,(1 - [kT/E_0 \ln(c/\upsilon)]^{1/2}) \qquad (2)$$

where the field sweeping rate is given by $\upsilon = dH/dt$, H_c^0 is the nucleation field at zero temperature, E_0 is roughly the nucleation barrier height at zero applied field and $c = H_c^0 kT/[2\tau_0 E_0\,(1 - H_c/H_c^0)]$. The validity of eq 2 was tested by plotting the set of $H_c(T,\upsilon)$ values as a function of $[T \ln(c/\upsilon)]^{1/2}$. If the underlying model is sufficient, all points should collapse onto one straight line by choosing the proper values for the constant τ_0. We found that the data of $H_c(T,\upsilon)$ with $T > 1$ K fell on a master curve provided $\tau_0 = 2.4 \times 10^{-7}$ s (Figure S11).

At lower temperatures, strong deviation from the master curves are observed. To investigate the possibility that these low-temperature deviations are due to escape from the metastable potential well by tunneling, a common method for classical models is to replace the real temperature T by an effective temperature $T^*(T)$ in order to restore the scaling plot.[56,62] In the case of tunneling, $T^*(T)$ should saturate at low temperatures. Indeed, the ansatz of $T^*(T)$, as shown in the inset of Figure S11 (bottom), can restore unequivocally the scaling plot demonstrated by a straight master curve [Figure S11 (bottom)]. The flattening of T^* corresponds to a saturation of the escape rate, which is a necessary signature of tunneling. The crossover temperature T_c can be defined as the temperature where the quantum rate equals the thermal one. The inset of Figure S11 (bottom) gives $T_c = 0.8$ K. The slope and the intercept of the master curves give $E_0/k_B = 40.3$ K and $H_c^0 = 3.8$ T.

This model can be used to find the field dependence of the effective energy barrier [eq 3] [56,57]

$$\Delta E = kT \ln(c/\upsilon)]) \qquad (3)$$

The result is plotted in Figure 8. One can see there how ΔE decreases with the increasing field. Below ca. 1.0 K, the tunneling reduces the barrier to zero.

In conclusion, the present detailed study of the slow relaxation of the chain **3** shows that the dynamics is Glauber-like at higher temperatures. Below ca. 3.0 K, a transition to finite size Glauber dynamics is observed. The presented low-temperature studies of the field-driven magnetization reversal for the low-temperature region suggest that the magnetization reversal starts by a quantum nucleation of a domain wall followed by domain wall propagation and reversal of the magnetization.

Monte Carlo Simulation of the Magnetic Properties of 4 and 5. The simulation of the magnetic properties is an important step for a correct analysis of the magnetic exchange in polynuclear compounds. Procedures based on the exact energy matrix diagonalization are commonly used to do this task, but their applicability is limited by the size of the systems, in particular in the case of the extended ones. Monte Carlo methods are well suited to analyze these latter systems, and they are among the most used ones to perform this work. In a classical spin approach, the implementation of the Monte Carlo algorithms (CMC) is a quite easy task.[63] Nevertheless, this approximation can be applied only to systems with large local spin values, such as high-spin iron(III) or manganese(II) complexes. In the cases of smaller spin values, the local spin moments have to be considered as quantum spins, and consequently, the so-called quantum Monte Carlo (QMC) methods must be used. The main drawbacks associated to the use of the QMC methods are their complexity and time consumption. The occurrence of low-spin iron(III) ($S_{Fe} = {}^1/_2$) in complexes **3**−**5**, leads us to use the QMC methods to simulate their magnetic properties. Among the possible QMC methods, we have chosen the decoupled Cell Monte Carlo method (DCM) which was proposed by Homma et al. and a modification of such approach from Miyazawa et al. that improves the results at low temperatures (mDCM).[64,65] These QMC methods are applied from the probability that implies a change in the m_s value (spin flip) for the site placed on the center of a cell or subsystem. This probability is evaluated by the exact diagonalization procedure

(55) Coulon, C.; Clérac, R.; Lecren, L.; Wernsdorfer, W.; Miyasaka, H. *Phys. Rev. B* **2004**, *69*, 132408.
(56) Wernsdorder, W.; Murugescu, M.; Tasiopoulos, A. J.; Christou, G. *Phys. Rev. B* **2005**, *72*, 212406.
(57) Wernsdorfer, W.; Clérac, R.; Coulon, C.; Lecren, L.; Miyasaka, H. *Phys. Rev. Lett.* **2005**, *95*, 237203.
(58) Stamp, P. C. E. *Phys. Rev. Lett.* **1991**, *66*, 2802.
(59) Chudnovsky, E. M.; Iglesias, O.; Stamp, P. C. E. *Phys. Rev. B* **1992**, *46*, 5392.
(60) Tatara, G.; Fukuyama, H. *Phys. Rev. Lett.* **1994**, *72*, 772.
(61) (a) Braun, H. B.; Kyriakidis, J.; Loss, D. *Phys. Rev. B* **1997**, *56*, 8129. (b) Ansermet, J. Ph.; Mailly, D. *Phys. Rev. B* **1997**, *55*, 11552.
(62) (a) Wernsdorfer, W.; Bonet Orozco, E.; Hasselbach, K.; Benoit, A.; Barbara, B.; Demoncy, N.; Loiseau, A.; Boivin, D.; Pascard, H.; Mailly, D. *Phys. Rev. Lett.* **1997**, *78*, 1791. (b) Wernsdorfer, W.; Bonet Orozco, E.; Hasselbach, K.; Benoit, A.; Mailly, D.; Kubo, O.; Nakano, H.; Barbara, B. *Phys. Rev. Lett*. **1997**, *79*, 4014.
(63) Cano, J.; Journaux, Y. *Magnetism: Molecules to Materials V*; Miller, J. S., Drillon, M., Eds.; Wiley: New York, 2004; Chapter 6.
(64) Homma, S.; Matsuda, H.; Ogita, N. *Prog. Theor. Phys.* **1986**, *75*, 1058.
(65) Miyazawa, S.; Miyashita, S.; Makivic, M. S.; Homma, S. *Prog. Theor. Phys.* **1993**, *89*, 1167.

applied to the mentioned subsystem. Thus, a better description of the spin correlation function is obtained for larger subsystem sizes, allowing the correct application of the method to lower temperatures. In the mDCM methods, the spin flip probability for the paramagnetic center i is calculated also, taking into account the neighboring subsystems involving it. Thus, the spin correlation function is more correct for the same subsystem size.

In the MC methods, from the spin flip probabilities and using a metropolis algorithm, we can generate a sampling where the states more present are those having a more important contribution in the partition function. This sampling allows us to calculate the average magnetization at a given temperature. The molar magnetic susceptibility can be obtained from the fluctuations in the magnetization through eq 4, where $\langle M \rangle$ and $\langle M^2 \rangle$ are the mean values of the magnetization and its square, and N, β, and k have their usual meaning.

$$\chi_M T = \frac{N\beta^2}{k(\langle M^2 \rangle - \langle M \rangle^2)} \tag{4}$$

In all simulations, the number of MC steps for each temperature is $5 \times 10^6/T$ (T in K). Thus, we included more steps in the sampling at low temperatures where the correct equilibrium requires more recorded data. Ten percent of the MC steps are employed for the thermalization of the system; thus, we stocked the physical properties when the equilibrium is reached. Models of 90 sites were used for compounds **4** and **5**. Periodic boundary conditions were introduced in all simulations. Deeper details on the MC simulations can be found in ref 63.

As mentioned above, low-spin octahedral iron(III) ions are present in **1**−**5**. The decrease of $\chi_M T$ in **1** and **2**, where no significant magnetic coupling is involved, is due to the spin−orbit coupling of the $^2T_{2g}$ ground term. Consequently, to simulate the magnetic behaviors of **3**−**5**, we have subtracted first the $\chi_M T$ data of **2** from those of **3**−**5** (per two iron atoms). Then, 0.91 cm^3 mol^{-1} K (Curie law term per two noninteracting spin doublets with $g = 2.20$, the g value being calculated from the extrapolated $\chi_M T$ value of **2** at 0 K) was added to the difference data. The procedure is expected to rule out the orbital contribution of the low-spin iron(III) to the magnetic behavior of **3**−**5**. However, the additional spin−orbit coupling contribution in **3** due to the presence of high-spin octahedral cobalt(II) ions precludes the simulation of the magnetic data of this compound. This is why we focused only on the QMC simulation of the corrected magnetic data of **4** and **5**.

We have applied the DCM and mDCM methods to a uniform 4,2-ribbonlike chain (only one exchange coupling parameter) where two different local spins occur [$S_{Fe} = {}^1/_2$ (**4** and **5**), $S_{Cu} = {}^1/_2$ (**4**), and $S_{Mn} = {}^5/_2$ (**5**)]. Ferro- (**4**) and ferrimagnetic (**5**) behaviors are observed. Only an intrachain coupling parameter and two decompositions in small cells were used in the simulations (Figure S12). Each decomposition was centered in different metal ions. For **4**, only the three first shells of neighbors were considered in the first decomposition, whereas the fourth nearest-neighbor shell was also introduced in the second one [Figure S12(a)]. However, smaller decompositions were considered for **5** [Figure S12(b)] because of the huge size of the issued energy matrix. Although the interaction topology in these systems is simple, the simulation of the experimental $\chi_M T$ vs T plots is a quite complex task due to the presence of a g-factor

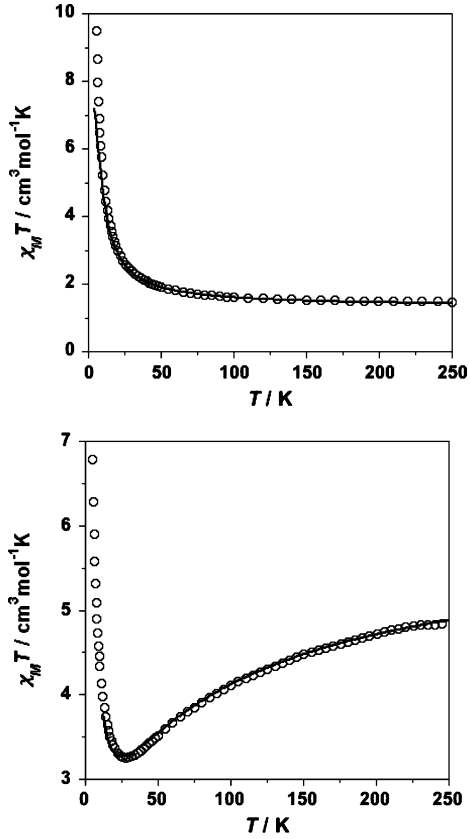

Figure 9. $\chi_M T$ vs T plots for **4** (top) and **5** (bottom): (○) experimental data; (–) simulated curve through QMC (see text).

for each metal ion. This last fact, that the g-factors take different values, not only modifies the values of $\chi_M T$ (including the value in the minimum when the exchange coupling is antiferromagnetic) but also causes a shift of the temperature of the minimum of $\chi_M T$. This last comment is visualized in a clearer way in Figure S13 where several sets of g values are displayed concerning the QMC simulations for **5** with an antiferromagnetic interaction between the local spins ($S_{Fe} = {}^1/_2$ and $S_{Mn} = {}^5/_2$). The temperature ranges of our QMC simulations are $T/|J| \geq 0.15$ (**4**) and 0.5 (**5**).

The simulated curves have been fitted to the corrected $\chi_M T$ vs T data, the best-fit parameters being $g_{Fe} = 2.20$, $g_{Cu} = 2.10$, and $J_{Fe-Cu} = +20.9$ cm^{-1} for **4** and $g_{Fe} = 2.20$, $g_{Mn} = 2.00$, and $J_{Fe-Mn} = -10.8$ cm^{-1} for **5** (see Figure 9). A good agreement between the simulated and experimental data is found in both cases. The nature of the magnetic interaction [ferro- (**4**) and antiferromagnetic (**5**)] is as expected, keeping in mind the symmetry of the interacting magnetic orbitals [t_{2g} vs e_g (**4**) and t_{2g} vs t_{2g}/e_g (**5**); see next section] but the values of the magnetic couplings in them are somewhat above from those reported for other magneto-structurally characterized single cyano-bridged Fe^{III} (low-spin)-Cu^{II} [J values of +5.0 and +12.6 cm^{-1} for $[\{Fe^{III}(phen)(CN)_4\}_2Cu^{II}(H_2O)_2]\cdot 4H_2O$ and $\{Fe^{III}_2Cu^{II}_2(\mu\text{-}CN)_4(bipy)_6\}(PF_6)_6\cdot 4CH_3CN\cdot 2CHCl_3$, respectively][12b,66] and Fe^{III} (low-spin)-Mn^{II} [J values of −1.3 and −3.0 cm^{-1} for $[\{Fe^{III}(bipy)(CN)_4\}_2Mn^{II}(H_2O)_4]\cdot 4H_2O$ and $(\mu\text{-bpym})[Mn^{II}(H_2O)_3\{Fe^{III}(bipy)(CN)_4\}_2]_2]\{Fe^{II}(bipy)(CN)_4\}_2\cdot 12H_2O$][15b,c] complexes.

(66) (a) Oshio, H.; Tamada, O.; Onodera, H.; Ito, T.; Ikoma, T.; Tero-Kubota, S. *Inorg. Chem.* **1999**, *38*, 5686. (b) Oshio, H.; Yamamoto, M.; Ito, T. *Inorg. Chem.* **2002**, *41*, 5817.

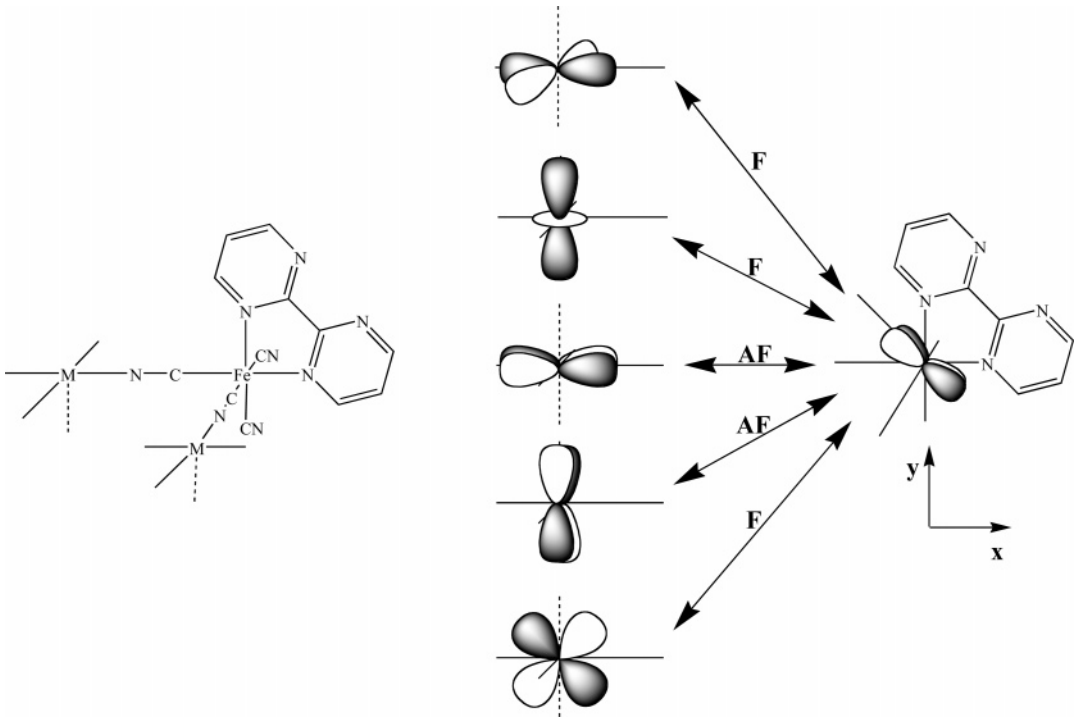

Figure 10. Orbital picture showing the different contributions to the magnetic coupling in a dinuclear fragment of **3**−**5** (F and AF stand for ferro- and antiferromagnetic couplings, respectively).

The different chromophore around the metal ions involved would account for the difference in the values of J.[67]

Analysis of the Exchange Pathways in 3−**5.** DFT calculations were used as a tool to elucidate the causes of the different magnetic behaviors observed in compounds **3**−**5** in the framework of the molecular orbital theory. These calculations also allowed us to evaluate the magnitude of the exchange coupling involved in each case. The $[Fe(bpym)(CN)_4]^-$ unit [see model **I** in Figure S14 (top)] that has a ground doublet spin state is present in compounds **2**−**5**. So, the first step was the treatment of this entity to get an orbital picture of the magnetic orbital (that is the molecular orbital which defines its unpaired electron). As in the similar $[Fe(phen)(CN)_4]^-$ building block (where bpym is substituted by phen) which was investigated in a previous work,[12b] the spin density map shows that its unpaired electron is described by a t_{2g}-type orbital. The spin density is mostly localized at the iron atom, the carbon and nitrogen atoms of the cyanide ligands presenting small spin densities whose sign is determined by the spin polarization mechanism. Having in mind the definition of the axes displayed in **I** [the x and y axes being roughly defined by the Fe−N(bpym) bonds], this magnetic orbital corresponds to the combination $d_{xz}-d_{yz}$ [see Figure S14 (bottom)]. The same procedure was applied to the $[M(CN)_4(H_2O)_2]^{2-}$ entity [M = Co (**3**), Cu (**4**), and Mn (**5**)]. The magnetic orbital in the copper unit corresponds to the $d_{x^2-y^2}$ (e_g), whereas the five 3d orbitals act as magnetic orbitals in the manganese one. The analysis for the cobalt unit is more complex, the two e_g ($d_{x^2-y^2}$ and d_{z^2}) and one t_{2g} (d_{xy}) orbitals playing the role of the magnetic orbitals.

With these results in mind, the prediction of the nature of the magnetic coupling in **3**−**5** is an easy task. Simple symmetry considerations allow the prediction of a positive value for the contributions to the magnetic coupling when the e_g magnetic orbitals of the divalent metal ion interact with the t_{2g} magnetic orbital of the iron(III) unit. This is a case of strict orthogonality between the magnetic orbitals [see Figure 10] across the bridging cyanide which is equatorially bound to the two metal ions. This case is exemplified by compound **4** which exhibits a ferromagnetic behavior. In compounds **3** and **5**, the occurrence of t_{2g} magnetic orbitals on the cobalt(II) and manganese(II) ions implies the addition of antiferromagnetic contributions which can be strong or practically nonexistent because of symmetry reasons according to the relative orientation of the magnetic orbitals. Due to the orientation of the magnetic orbital of the low-spin iron(III) ion (the value of the angle between the plane that encompasses it and the z axis is close to 45°), only moderate antiferromagnetic (one ($t_{2g} - t_{2g}$) term) and ferromagnetic (two ($t_{2g} - e_g$) terms) contributions are expected (Figure 10) in **3**. The single antiferromagnetic contribution in this compound is not able to cancel the two ferromagnetic terms, and a net ferromagnetic interaction results, as evidenced experimentally. The occurrence in **5** of additional ($t_{2g} - t_{2g}$) antiferromagnetic contributions leads to a net antiferromagnetic interaction in agreement with its ferrimagnetic behavior.

In previous works with cyano-bridged systems, we have observed that density functional calculations provide a good qualitative evaluation of the exchange coupling constants.[12b,16a,68] However, from a quantitative point of view, the calculated magnetic couplings are overestimated. In this respect, we have concluded that the presence of the charged terminal cyanide ligands (especially in the models where the one-dimensional system is cut, generating a greater number of these ligands) is responsible for the problem in the correct convergence of

(67) Román, P.; Guzmán-Miralles, C.; Luque, A.; Beitia, J. I.; Cano, J.; Lloret, F.; Julve, M.; Alvarez, S. *Inorg. Chem.* **1996**, *35*, 3741.

(68) Lescouëzec, R.; Toma, M. L.; Toma, L. D.; Vaissermann, J.; Verdaguer, M.; Delgado, F. S.; Ruiz-Pérez, C.; Lloret, F.; Julve, M. *Coord. Chem. Rev.* **2005**, *249*.

calculations and the overestimation of the exchange coupling constants. Although the substitution of cyano groups by ammonia ligands minimizes both problems, it is not enough. A different strategy has been used in the present work. Here we have taken a more extended model which is closer to the 4,2-ribbonlike chain (see **II** in Figure S15). In this model, two iron(III) ions are at the center, and three coordination shells (the first, second, and third metal neighbors) are considered. To simplify the calculations, and taking advantage of the crystal structure of **2**, the third metal neighbor shell is substituted by the diamagnetic zinc(II) ions using the experimental metal-to-ligand distance observed in this compound. With this model, the influence in the modelization on the centered metal ions is minimized. So, the two calculated configurations are the one displaying all local spins aligned in a ferromagnetic manner (Φ_F) and the other one where the spin moments of the centered iron(III) ions are opposite to the rest (Φ_{AF}) [Figure S15(b)]. The spin density map for the most stable configuration of the chain **5** (with local spins arranged in an antiferromagnetic manner) is shown in Figure S16. One can see there the spherical distribution of the spin density around the manganese atom and the perpendicular arrangement of the spin density of the iron atom with respect to the bpym mean plane in agreement with the DFT calculations done for model **I**. Note that the expression used for the evaluation of the exchange coupling constants is given in eq 5:

$$J = \frac{E(\Phi_F - \Phi_{AF})}{4n} \tag{5}$$

with $n = 2$, 1, and 3 for **3**, **4**, and **5**, respectively.

The calculated results are: $J_{Fe-Co} = +6.1$ cm^{-1}, $J_{Fe-Cu} = +62.9$ cm^{-1}, and $J_{Fe-Mn} = -11.7$ cm^{-1}. They agree qualitatively with the experimental ones. However, the overestimation of the values of J remains. Although this overestimation here is reduced when compared to the results in our previous works, due to a better choice of the model, it is not enough for an accurate evaluation. To improve this situation, studies with similar models immersed in a dielectric to simulate the remaining solid are in progress.

Concluding Remarks

In this paper, the crystal structure of the mononuclear precursor $PPh_4[Fe(bpym)(CN)_4]\cdot H_2O$ (**1**) and those of the bimetallic chains $\{[Fe^{III}(bpym)(CN_4)]_2M^{II}(H_2O)_2\}\cdot 6H_2O$ [M = Zn (**2**), Co (**3**), Cu (**4**), and Mn (**5**)] have been determined, and their magnetic behaviors have been investigated as a function of the temperature. Compounds **3** and **4** exhibit intrachain ferromagnetic couplings and weak interchain antiferromagnetic interactions, whereas compound **5** is a ferrimagnetic chain. DFT-type calculations and the Monte Carlo methodology allowed us to analyze the exchange pathways involved and also to simulate the magnetic data. Both dc and ac magnetic measurements demonstrate that compound **3** behaves as a SCM, this compound being the first example of SCM obtained with the use of the new low-spin iron(III) complex $[Fe(bpym)(CN)_4]^-$ as a ligand toward fully solvated transition metal ions. This bottom-up synthetic strategy appears to be a safe route to design SCMs with intrachain ferromagnetic coupling. Interestingly, the detailed study of the slow relaxation of the magnetization of the bimetallic chain **3** shows that its magnetization reversal in the low-temperature region starts by a quantum nucleation of a domain wall followed by domain wall propagation and reversal of the magnetization. Complex **3** is the second example of SCM which exhibits quantum effects.

Acknowledgment. This work was supported by the European Union through the Network QueMolNa (Project MRTN-CT-2003-504880) and the Magmanet Network of Excellence (Contract 515767-2), el Ministerio Español de Educación y Ciencia (Project CTQ2004-03633 and MAT2004-03112), the Generalitat Valenciana (Grupos 03/197), and the Gobierno Autónomo de Canarias (PI2002/175). Two of us (J.P. and L.M.T.) thank the Ministerio Español de Educación for predoctoral fellowships.

Supporting Information Available: Cystallographic tables (Tables S1−S4), additional structural drawings (Figures S1−S4), magnetic plots (Figures S5−S13), models for the theoretical calculations (Figures S14 and S15), spin density map for the model **II** of **5** (Figure 16) and X-ray crystallographic files (CIF) for **1**−**5** and complete ref 46. This material is available free of charge via the Internet at http://pubs.acs.org. The crystallographic files are also available on application to the Cambridge Data Centre, 12 Union Road, Cambridge CB21EZ, U.K. (Fax: (+44) 1223-336-033; e-mail: deposit@ccdc.cam.ac.uk), CCDC 259180 (**1**), 259181 (**2**), 259182 (**3**), 259183, (**4**) and 259184 (**5**).

JA058030V